Tracking Brownian motion in three dimensions and characterization of individual nanoparticles using a fiber-based high-finesse microcavity

Larissa Kohler (larissa.kohler@kit.edu)
Karlsruhe Institute of Technology
Matthias Mader
Ludwig-Maximilians-Universität München
Christian Kern
Karlsruher Institut für Technologie
Martin Wegener
Karlsruhe Institute of Technology
David Hunger
Karlsruhe Institute of Technology https://orcid.org/0000-0001-6156-6145

Article

Keywords: Dynamics of Nanosystems in Solution, Dispersive Frequency Shifts, Polarizability, Hydrodynamic Radius, Effective Refractive Index

Posted Date: October 20th, 2020

DOI: https://doi.org/10.21203/rs.3.rs-86943/v1

Version of Record: A version of this preprint was published at Nature Communications on November 4th, 2021. See the published version at https://doi.org/10.1038/s41467-021-26719-5.

Tracking Brownian motion in three dimensions and characterization of individual nanoparticles using a fiber-based high-finesse microcavity

Larissa Kohler,[1] Matthias Mader,[2,3] Christian Kern,[4,5] Martin Wegener,[4,5] and David Hunger[1,6,*]

[1] *Karlsruher Institut für Technologie, Physikalisches Institut, Wolfgang-Gaede-Str. 1, 76131 Karlsruhe, Germany*
[2] *Fakultät für Physik, Ludwig-Maximilians-Universität, Schellingstraße 4, 80799 München, Germany*
[3] *Max-Planck-Institut für Quantenoptik, Hans-Kopfermann-Str. 1, 85748 Garching, Germany*
[4] *Karlsruher Institut für Technologie, Institut für Angewandte Physik, Wolfgang-Gaede-Str. 1, 76131 Karlsruhe, Germany*
[5] *Karlsruher Institut für Technologie, Institut für Nanotechnologie, Hermann-von-Helmholtz-Platz 1, 76344 Eggenstein-Leopoldshafen, Germany*
[6] *Karlsruher Institut für Technologie, Institut für QuantenMaterialien und Technologien , Hermann-von-Helmholtz-Platz 1, 76344 Eggenstein-Leopoldshafen, Germany*[*]

The dynamics of nanosystems in solution contains a wealth of information with relevance for diverse fields ranging from materials science to biology and biomedical applications. When nanosystems are marked with fluorophores or strong scatterers, it is possible to track their position and reveal internal motion with high spatial and temporal resolution. However, markers can be toxic, expensive, or change the object's intrinsic properties. Here, we simultaneously measure dispersive frequency shifts of three transversal modes of a high-finesse microcavity to obtain the three-dimensional path of unlabeled SiO_2 nanospheres with 300 µs temporal and down to 8 nm spatial resolution. This allows us to quantitatively determine properties such as the polarizability, hydrodynamic radius, and effective refractive index. The fiber-based cavity is integrated in a direct-laser-written microfluidic device that enables the precise control of the fluid with ultra-small sample volumes. Our approach enables quantitative nanomaterial characterization and the analysis of biomolecular motion at high bandwidth.

The development of optical sensors for the detection and analysis of unknown nanomaterials and their motional dynamics is of great importance. With fluorescence microscopes it is possible to get spatial information beyond the diffraction limit and to resolve fluorophores down to the nanometer scale [1–3]. Their further development enables the tracking of individual nanosystems [4–6]. Without labeling, it is possible to track nanosystems by the detection of the Rayleigh-scattered light using interference techniques to extract the weak signal from the background noise [7, 8]. The weak signals enforce the integration over time or the labeling of the nanosystem with a strong scatterer to reach better temporal resolution [9]. Other approaches which enable single nanoparticle detection are evanescent biosensors using e.g. nanoplasmonics [10, 11], tapered fibers [12], or whispering gallery mode resonators such as microspheres [13, 14], which enable the real-time detection of frequency changes [15–18] and quantitative particle sizing [19]. However, those sensors are limited to the evanescent near-field. To achieve the monitoring of unconstrained diffusive motion, sensing of nanosystems far away from the sensor surface is desired. Open-access microcavities have recently been introduced as a promising alternative platform for refractive index sensing [20] or nanoparticle trapping [21]. The full access to the cavity mode allows for optimal overlap of the sample with the cavity mode and enables quantitative nanoparticle characterization. So far, focused-ion-beam milled structures on planar substrates have been used, with the challenge to provide controlled flow through a specific cavity, the need for free space optics, and limited cavity finesse. Furthermore, as a general aspect, cavity-enhanced measurements typically rely on probing isolated resonances which do not provide much spatial information about the sample. Exceptions are scanning microcavities [22, 23], but they are not capable to track the fast Brownian motion of nanosystems, or cavities with special geometries that lead to degenerate transverse modes [24, 25], that can have imaging capabilities, however, they lack sensitivity for nano-scale samples. It is therefore highly desirable to extend the capability of microcavities for ultra-sensitive quantitative characterizations towards the analysis of motional dynamics and position tracking to achieve a boost in sensitivity for studies of unlabeled nanosystems.

Here, we use a high-finesse open-access microcavity to demonstrate quantitative nanoparticle characterization and introduce a novel technique to perform three-dimensional position tracking of nanoparticles dispersed in water. The device is long-term stable such that we can obtain an extended statistics from several hundred single-particle transits. This allows us to measure the particles' polarizability and the temporal variation of the sample over time. If the particle size is measured in addition, its effective refractive index can be determined. Therefore, we introduce a novel scheme for particle tracking. By simultaneously measuring the frequency shifts of three different transverse modes of the cavity, we are able to

* david.hunger@kit.edu

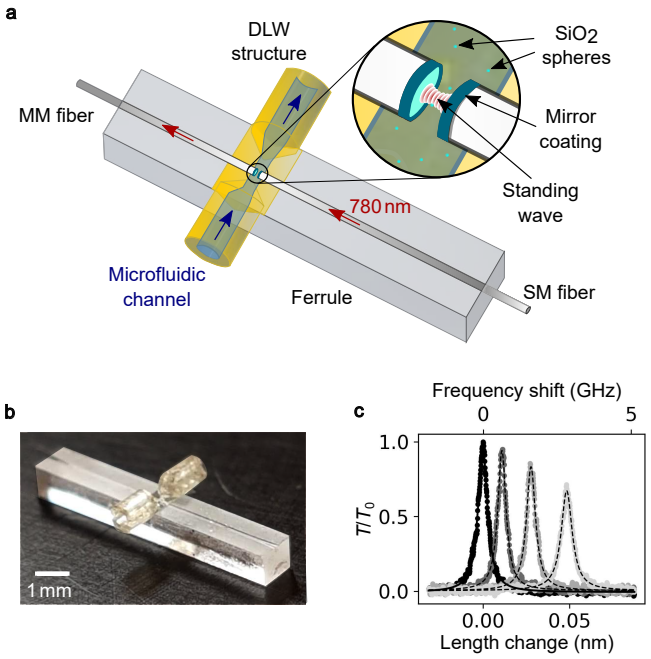

FIG. 1. **Fabry-Pérot microcavity device and measurement signal.** (a) Schematic setup showing the cavity and its integration into a glass ferrule with a direct-laser-written (DLW) structure (yellow) forming the microfluidic channel. b) Picture of the microfluidic device. c) Examples of the cavity transmission signal for an empty cavity (black) and with nanoparticles present at increasing spatial overlap with the cavity mode (decreasing gray value). The increasing frequency shift, decreasing peak transmission, and increasing linewidth are visible.

infer the instantaneous three-dimensional coordinates of a nanoparticle and resolve its trajectory. From a single transient track we can deduce the particles diffusivity and thereof its hydrodynamic radius, such that together with the measured polarizability, we can infer the key dispersive properties of individual nanoparticles. Particle tracking adds a central functionality to cavity-based sensing, opening up prospects for studies of diffusion dynamics and accurate characterizations of molecular systems.

Results

Integrated microfluidic cavity setup. Our Fabry-Pérot cavity system is based on two laser-machined and mirror-coated optical fibers that form a microcavity between the two fiber end facets [26, 27], see Fig. 1a. The fibers are inserted into a precision ferrule for lateral alignment and are mounted on shear piezo-electric actuators outside the ferrule (see Supplementary Fig. 1) for fine-tuning of the mirror separation and thereby the cavity resonance condition. The cavity standing wave is located in a microfluidic channel, which is defined by a 3D laser-written polymer structure (see Supplementary Fig. 2) that forms a 200 µm-diameter channel transversing the cavity, thus allowing for a laminar, precisely controllable flow through the microfluidic device, see Fig. 1b. The cavity can be probed by coupling light into the single-mode (SM) fiber, and we detect the transmitted light emerging from the cavity through a multi-mode (MM) fiber. When operated in air, the cavity finesse is as high as $\mathcal{F} = 90000$, while when immersed in distilled an filtered water, we observe a finesse of up to $\mathcal{F} = 56710$ and a mode waist as small as $w_0 = 1.5\,\mu\text{m}$. The reduced Finesse in water is expected and consistent with the change in mirror reflectivity due to the higher refractive index of water compared to air, and the absorption loss in water. The figure of merit for the sensitivity of this cavity, $\mathcal{C} \propto Q/V \propto \mathcal{F}/(\pi w_0^2)$, is comparable to those of optimized WGM resonators, but with the advantage of a fully accessible cavity mode which avoids modification of the cavity due to binding events, and which permits the observation of free, unconstrained diffusion. Furthermore, the cavity resonance can be tuned to a desired wavelength, e.g. to match that of the probe laser, or can be used for cavity-enhanced spectroscopy. In the experiments described below, we probe the cavity with a grating-stabilized diode laser of wavelength $\lambda = 780\,\text{nm}$ and detect the transmitted light by an avalanche photodetector. The cavity length is modulated at a frequency of $3 - 10\,\text{kHz}$ to repeatedly sample the fundamental cavity resonance. For each occurring resonance, we measure the location and amplitude of the peak to infer the cavity frequency shift and the transmitted power as a function of time (see Supplementary Fig. 4). For all experiments, we flooded the microfluidic cell with the nanoparticles dispersed in double distilled water and then turned the pressure off to stop the flow. After 10 min to 1 h of waiting time we started the measurements. Fig. 1c exemplarily shows snapshots of the cavity transmission signal when a single nanoparticle enters the cavity with increasing spatial overlap with the cavity mode. In the following, we present results which were measured by two different cavity setups (1,2) with two different samples (A,B) (see Supplementary Note 1).

Single nanoparticle sensing and quantitative analysis. We investigate SiO_2 nanospheres with a narrow size distribution (sample A: radius $63 \pm 2\,\text{nm}$, sample B: $60 \pm 2\,\text{nm}$) as a model system to characterize and calibrate our device. When a nanosphere enters the cavity standing wave light field with normalized intensity distribution I_{cav} and cavity mode volume V_{mode}, its polarizability $\alpha = 4\pi r^3 \epsilon_0 (n_{\text{p}}^2 - n_{\text{m}}^2)/(n_{\text{p}}^2 + 2n_{\text{m}}^2)$ produces a relative frequency shift $\Delta\nu/\nu = \alpha(\int_{V_{\text{NP}}} I_{\text{cav}} dV_{\text{NP}})/(2\epsilon_0 V_{\text{mode}})$ of the cavity resonance. The amount of shift depends on the electrical field strength penetrating the nanosphere and is therefore maximal at the antinode and minimal but non-zero at the node since the nanosphere has a non-negligible extension. In addition, the non-absorbing SiO_2 nanosphere leads to a decrease of the cavity peak transmission due to additional loss from Rayleigh scatter-

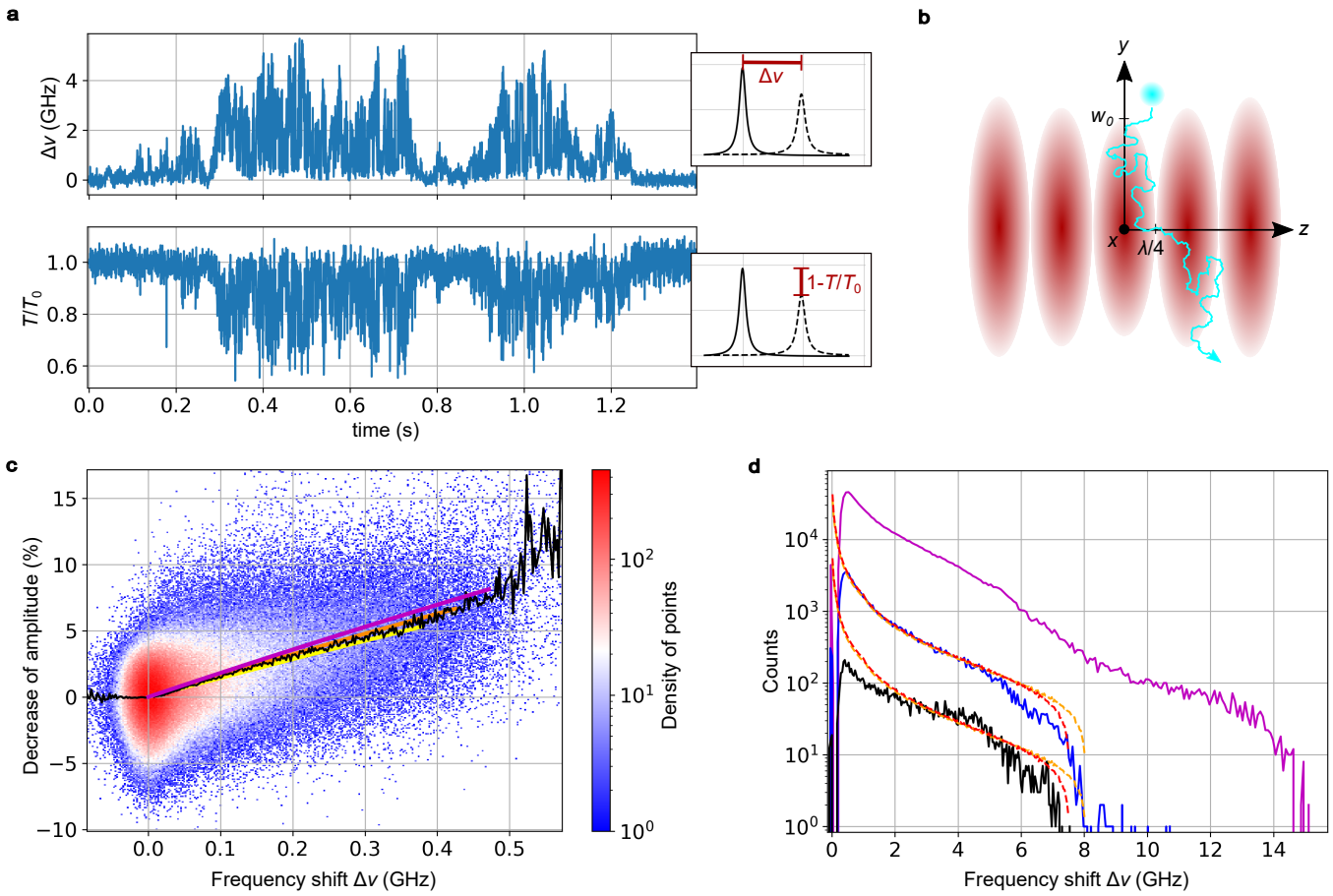

FIG. 2. **Quantitative nanoparticle characterization.** a) Cavity frequency shift and peak transmission amplitude as a function of time produced by a single SiO_2 nanoparticle. b) Schematic sketch of a nanoparticle diffusing through the standing wave cavity field. c) Statistical correlation of cavity frequency shifts and transmission reductions. Solid black line: Mean transmission reduction for a given frequency shift. Solid yellow line: simulation for $n_\mathrm{p} = 1.41$, orange: $n_\mathrm{p} = 1.42$; purple: $n_\mathrm{p} = 1.43$. d) Histograms for the measured frequency shifts of a single transit event (black data) shown in Fig. 3b, 59 transits (blue data, measurement duration: 2 hours) and 210 additional transits (magenta data, 8 hours). The observed increased shifts reveal agglomeration. Dashed lines: simulation for $n_\mathrm{p} = 1.46$ and the mean radius of $r_\mathrm{hydr} = 75.3\,\mathrm{nm}$ (red) and the maximal radius of $r_\mathrm{hydr} = 77.2\,\mathrm{nm}$ (orange).

ing, $S = |\alpha|^2 k^4/(6\pi\epsilon_0^2)$. Fig. 2a shows an exemplary time trace of the cavity resonance shift and the corresponding transmission change produced by a single nanoparticle (sample B, cavity 2, see Supplementary Fig. 5 for details on data evaluation). The fluctuations emerge from the particle's Brownian motion through the standing-wave cavity field as schematically depicted in Fig. 2b. We can measure many such events and correlate the frequency shift and the transmission change as depicted in Fig. 2c. Here, the data of 330 transit events are shown (sample A, cavity 1). A histogram of the time duration of individual transit events yields an average dwell time of 0.47 s (see Supplementary Fig. 6). Notably, the transmission change and the frequency shift signals depend on the cavity mode geometry in the same way, such that the slope of the signal is independent of it. This allows us to evaluate the polarizability in a quantitative manner that is immune against systematic errors of the cavity geometry. If furthermore the particle size is known or measured (see section particle tracking), one can infer the refractive index of the material. For this purpose, we compare the observed mean values of the correlation signal with the expected signal for a spherical particle with the size given by the manufacturer and use the refractive index as a free fit parameter (see Supplementary Note 2). From this, we can precisely determine the effective refractive index, and for a nanoparticle radius of $r_\mathrm{hydr} = 71.5\,\mathrm{nm}$ we find $n_\mathrm{p} = 1.41 \pm 0.01$ (see Supplementary Fig. 7), which is in good agreement with the value provided by the manufacturer ($n_\mathrm{p} = 1.42$, sample A).

When a single nanoparticle diffuses in the cavity light field, the probability to transit through the electric field maximum and accordingly to produce the maximal frequency shift is small. This can be quantified by the den-

sity of states of available positions that produce a certain frequency shift (see Supplementary Note 3). Fig. 2d shows histograms of frequency shifts from nanoparticle events, which were measured successively without changing the nanoparticle solution inside the microfluidic cell in between. The histograms can be fitted by the modeled density of states with the refractive index as the only free parameter (sample B, cavity 2). Already for a single nanoparticle transit (black data), a good agreement is found and the polarizability or the refractive index (if r_{hydr} is known) can be inferred. The statistics improves for intermediate measurement times, and averaging over 59 transits yields the best agreement with $n_{\mathrm{p}} = 1.46 \pm 0.01$ (blue data). This result for the refractive index is consistent with the expected value for sample B (see Supplementary Fig. 10). More details are given in Supplementary Fig. 8. For measurement times longer than two hours, we observe an increase in larger frequency shifts, extending to values up to two times larger than the expected maximum single particle frequency shift (yellow data). This observation is consistent with continuous adsorption of molecular layers on the nanoparticles, or with agglomeration of nanoparticles into dimers. This analysis allows us to monitor temporal changes of the sample properties in a sensitive manner.

For the calculation of the refractive index in Fig. 2d we measured the value for the nanoparticle radius of $r_{\mathrm{hydr}} = 75.3 \pm 2\,\mathrm{nm}$ in aqueous solution by dynamic light scattering (DLS), hence representing the hydrodynamic radius, which is 15.3 nm larger than the geometric radius of the solid glass sphere of $r_{\mathrm{SiO2}} = 60.0 \pm 2\,\mathrm{nm}$, which was obtained from transmission electron micrographs (see Supplementary Fig. 10). When assuming that our data originates only from the SiO_2 nanosphere with $r_{\mathrm{SiO2}} = 60\,\mathrm{nm}$, the observed frequency shifts would correspond to a refractive index of $n_{\mathrm{p}} = 1.59$, noticeably larger than the refractive index of the SiO_2 bulk material (1.45 at 780 nm). From this analysis, we conclude that our cavity sensor is sensitive to the hydrodynamic particle size [12]. With the above results, we can calculate the effective refractive index of the hydration shell to be $n_{\mathrm{h}} = 1.46 \pm 0.01$. Analogous evaluations for sample A yield a hydrate shell with 8.5 nm thickness and $n_{\mathrm{h}} = 1.40 \pm 0.04$. This analysis shows that our measurement technique allows us to quantify properties of the hydration shell.

Particle Tracking.

As a next step, we introduce a method to achieve *three-dimensional* tracking of nanoparticle motion within the cavity. Therefore, we make use of the signal of two higher-order transverse modes in addition to the fundamental cavity mode. To reduce the required amplitude for the cavity length modulation, we use two lasers with different wavelengths such that the fundamental mode probed by laser 1 appears in the middle of the frequency-split TEM_{01}/TEM_{10} modes which are probed by laser 2. Fig. 3a shows a cavity transmission measurement of the three modes together with their lateral intensity distributions. The modes have complementary spatial distributions, leading to a unique set of corresponding frequency shifts produced by a nanoparticle at any given position inside the light field. Due to symmetry, this uniqueness is limited to one octant of a cartesian coordinate system that is centered at one field antinode, such that the assignment of spatial positions will be folded into this domain. However, this does not alter the properties of the inferred Brownian motion, and effects such as anisotropy or reduced dimensionality of diffusion would remain visible.

Using cavity 2, we measured several hundred transit events with the three modes at the same time (see Supplementary Note 1). Fig. 3b shows a representative time trace for a single nanoparticle (sample B) entering the cavity mode multiple times (see Supplementary Fig. 13 for detailed evaluation). One can see the different behavior of the three modes depending on the nanoparticle's position inside the cavity light field. In Fig 3c, the corresponding positions are schematically sketched for different times marked in orange in Fig. 3b. The frequency shift distribution of the fundamental mode is shown in Fig. 2d (black line), those for the higher order modes are shown in Supplementary Fig. 12, and all three distributions are consistent with a single nanoparticle. To obtain the most probable nanoparticle position for a given time, we compare the measured frequency shift triples with simulated shifts for all possible nanoparticle positions (see Supplementary Note 3 and 4). Due to the present measurement noise for each mode (see Supplementary Fig. 14), multiple positions are compatible with the measured shifts. We constrain the choice by demanding that subsequent positions have the smallest spatial separation. This gives the three-dimensional coordinates of the nanoparticle for each measurement time (see Fig. 3d). Fig. 3e shows the nanoparticle movement in the three-dimensional space for the time interval marked in red in b) and d). In the current measurement, we reach a signal-to-noise ratio of SNR = 51, which is the quantity that determines the uncertainty of the localization. Fig. 3f shows the localization uncertainties in the xz- and xy-plane for $y = 0$ and $z = 0$ respectively. We define the localization uncertainty as $\delta r = (\delta x \delta y \delta z)^{1/3}$ from the respective coordinate range that is compatible with the measurement including the noise. The minimal localization uncertainty is found to be 8 nm at the points of largest intensity gradients, and the mean uncertainty within the sensing volume which extends up to the $1/e^2$ contour of the standing wave is 44 nm.

We are able to deduce the diffusivity as well as the nanoparticle size from the track by calculating the mean squared displacement for the x,y-direction (see Supplementary Fig. 16). Since the sensing volume extension in z-direction ($\lambda/4 = 0.15\,\mathrm{nm}$) is much smaller than in x,y-direction ($w_0 = 1.5\,\mu\mathrm{m}$) and the mean localization uncertainty (see below) is on a similar order as the z-extension, only the x,y-coordinates of the transit event are used for the evaluation. This gives a mean diffusivity

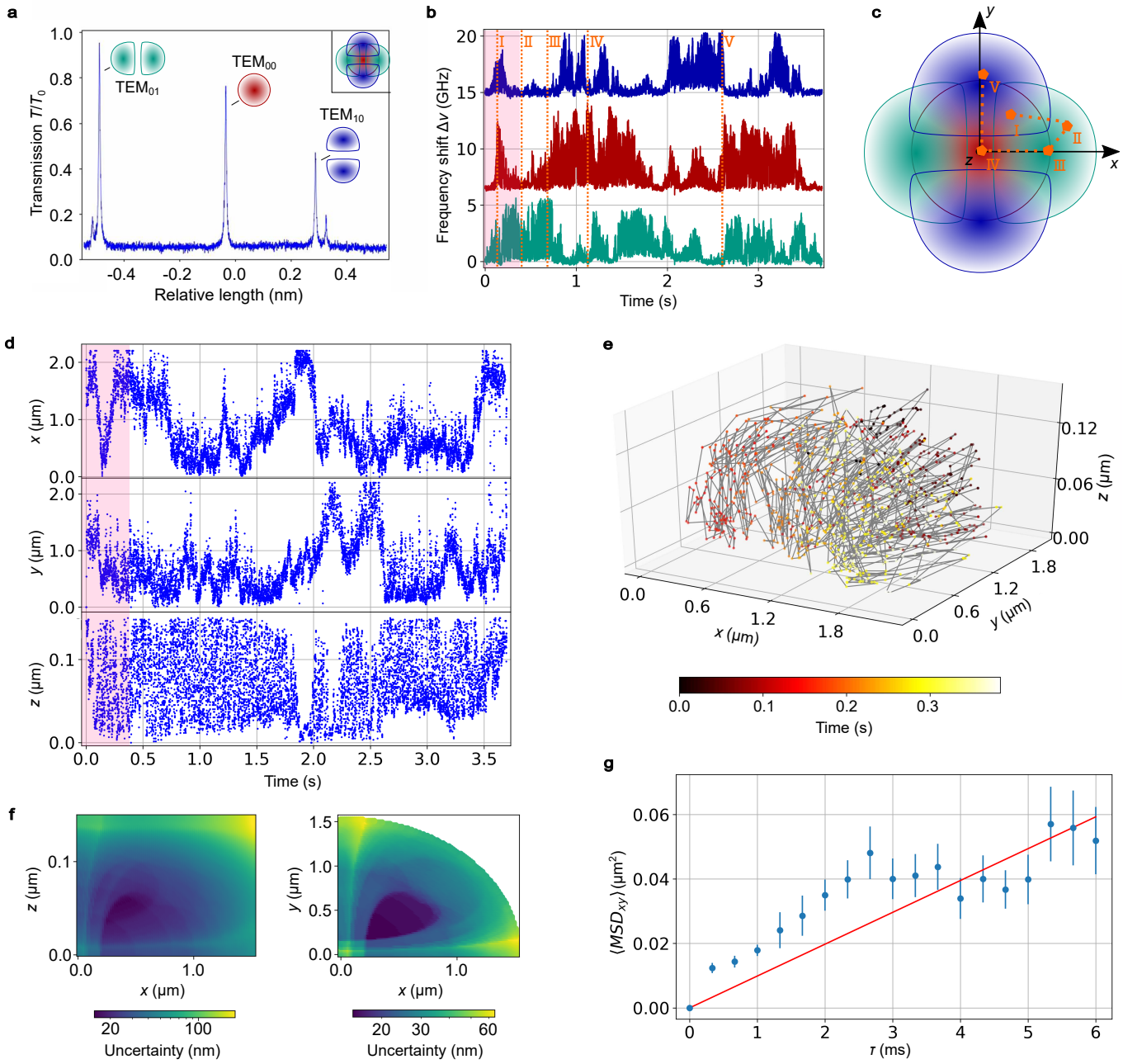

FIG. 3. **Three-dimensional tracking of a single SiO_2 nanosphere and determination of its diffusivity.** a) Cavity transmission signal with the three evaluated modes indicated. Inset: Schematic illustration of the complementary spatial regions covered by the modes. b) Time trace of frequency shifts of the three modes. c) Sketch for different particle positions at different times depicted in 3b) d) Evaluated positions for shortest distance algorithm. e) Two-dimensional representation of the position tracking. f) Lateral resolution for different positions. g) Mean squared displacement for the lateral diffusion and weighted linear fit. The error bars represent the standard deviation.

of $\langle D \rangle = 2.5 \cdot 10^{-12} \pm 0.7 \cdot 10^{-12}\,\mathrm{m}^2/\mathrm{s}$ and a hydrodynamic radius 86.9 $\pm$ 23.6 nm, which is in good agreement with the size distribution determined via DLS measurements (see Supplementary Fig. 10).

As an important result of this analysis, the particle tracking allows us to infer the hydrodynamic radius of a single nanoparticle, while from the frequency shift probability distribution (see Fig. 2d) we obtain the polarizability. Measuring the cavity transmission change in addition provides a higher precision and makes the measurement immune against e.g. systematic errors in the cavity geometry. Combining only these two measurements, which can be performed at the same time, we can deduce the effective refractive index of a single nanoparticle.

Discussion

Our work demonstrates a compact and robust ultra-sensitive microcavity sensor that has shown stable operation over several weeks in a given configuration and is thus useful for extensive studies. We have introduced the simultaneous measurement of several cavity transverse modes to achieve three-dimensional particle tracking inside the cavity, which is an important step to combine the exceptional sensitivity of cavity-based sensors with spatial imaging. This could be used to achieve a quantitative characterization of the nanoparticle size and effective refractive index. The noise level of the current measurements would allow the investigation of particles with hydrodynamic radii down to 20 nm. Significant further improvements in sensitivity are expected by active stabilization of the cavity, smaller mode volumes, and noise-rejection techniques such as heterodyne spectroscopy, such that few-nm large biomolecules can be expected to become detectable. Increased SNR and further optimization e.g. with Bayesian analysis [6] could offer improved precision for position tracking. Operating under active stabilization allows one to harness the full bandwidth of the sensor, which in principle is bounded only by the cavity decay rate of $\sim 10^8$ Hz. This could enable the label-free study of dynamical processes of biologically relevant processes such as protein folding on a single molecule level.

Methods

Experimental set-up. Our measurements were taken with two different cavity configurations (cavity 1 and 2). The following parameters were determined for the cavities filled with water. Cavity 1 had a Finesse of 18400, an effective cavity length of 27.3 µm and the mirrors had a mean central radius of curvature of $r_{\mathrm{c,SM}} = 59.3\,\mu\mathrm{m}$ and $r_{\mathrm{c,MM}} = 94.5\,\mu\mathrm{m}$. Cavity 2 had a Finesse of 56710 at the effective cavity length of 5.4 µm. Here we used mirrors with $r_{\mathrm{c,SM}} = 49.6\,\mu\mathrm{m}$ and $r_{\mathrm{c,MM}} = 83.5\,\mu\mathrm{m}$. The effective cavity length $d = d_{\mathrm{g}} + d_{\mathrm{p}}$ in water is given by the mirror separation d_{g} and the field penetration length d_{p} which can be as small as $d_p = 430\,\mathrm{nm}$ and defines together with the radius of curvature the mode radius $w_0 = 2.3\,\mu\mathrm{m}$ and the mode volume $V_{\mathrm{m}} = 110.0\,\mu\mathrm{m}^3$ for cavity 1 and $w_0 = 1.5\,\mu\mathrm{m}$ and $V_{\mathrm{m}} = 10.0\,\mu\mathrm{m}^3$ for cavity 2. The quality factor depends on the mirror separation. Here it is $Q = 1.7 \cdot 10^6$ for cavity 1 and $Q = 1.0 \cdot 10^6$ for cavity 2. In the quantitative measurements, we use a grating-stabilized diode laser at 780 nm to probe the cavity, and detect the transmitted light by a photodetector (see Supplementary Fig. 1). We modulate the cavity length at a frequency of 3 - 10 kHz with an amplitude of 150 pm to repeatedly sample the cavity fundamental mode.

Data analysis. The high frequency signals are recorded by an oscilloscope which is operated in sequence mode. From the resonance curve of each trigger event the amplitude and the time position of the amplitude in relation to the trigger is extracted (see Supplementary Fig. 4). In order to remove cavity drifts (mainly thermal expansion) from the frequency shift data, we subtract parabolas fitted to the background noise (see Supplementary Fig. 5).

Nanoparticles. We use silicon dioxide nanoparticles from two different companies: SiO_2 spheres with a hydrodynamic radius of $r_{\mathrm{hydro}} = 71.5\,\mathrm{nm}$, a standard deviation of $\sigma = 2\,\mathrm{nm}$ and a refractive index of $n_{\mathrm{SiO2}} = 1.42$ from microparticles GmbH (sample A). SiO_2 spheres with a geometric radius of $r = 60\,\mathrm{nm}$ and $\sigma < 2.2\,\mathrm{nm}$ from ALPHA Nanotech (sample B). More information can be taken from Supplementary Fig. 9 and 10.

ACKNOWLEDGMENTS

This work was partially funded by the Deutsche Forschungsgemeinschaft (DFG), the Cluster of Excellence Nanosystems Initiative Munich (NIM) and the Karlsruhe School for Optics and Photonics (KSOP). It was supported by the Laser Material Processing (LMP) infrastructure of the Karlsruhe Nano Micro Facility (KNMF), a Helmholtz Research Infrastructure at Karlsruhe Institute of Technology (KIT). We thank L. Radtke, P. Brenner, M. Schumann and M. Rutschmann, for experimental assistance and T. Hümmer, M. Hippler and T. W. Hänsch for helpful discussions.

AUTHOR CONTRIBUTIONS

L.K., M.M. and D.H. conceived the original idea, L.K. performed theoretical calculations, L.K. and C.K. prepared the experimental set-up, L.K. performed the experiments and analysed the data, all authors discussed the results, L.K. and D.H. wrote the manuscript, and all authors provided feedback.

ADDITIONAL INFORMATION

REFERENCES

[1] E. Betzig, G. H. Patterson, R. Sougrat, O. W. Lindwasser, S. Olenych, J.S. Bonifacino, M. W. Davidson, J. Lippincott-Schwartz, and H. F. Hess. Imaging intracellular fluorescent proteins at nanometer resolution. *Sci-*

ence, 313(5793):1642–1645, 2006.

[2] W. E. Moerner and D. P. Fromm. Methods of single-molecule fluorescence spectroscopy and microscopy. *Review of Scientific Instruments*, 74(8):3597–3619, 2003.

[3] Y. Sonnefraud, H. G. Sinclair, Y. Sivan, M. R. Foreman, C. W. Dunsby, M. A. A. Neil, P. M. French, and S. A. Maier. Experimental proof of concept of nanoparticle-assisted STED. *Nano Letters*, 14(8):4449–4453, 2014.

[4] Y. Eilers, H. Ta, K. C. Gwosch, F. Balzarotti, and S. W. Hell. MINFLUX monitors rapid molecular jumps with superior spatiotemporal resolution. *Proceedings of the National Academy of Sciences of the United States of America*, 115(24):6117–6122, 2018.

[5] K. McHale and H. Mabuchi. Precise characterization of the conformation fluctuations of freely diffusing DNA: Beyond rouse and zimm. *Journal of the American Chemical Society*, 131(49):17901–17907, 2009.

[6] C. Limouse, J. C. Bell, C. J. Fuller, A. F. Straight, and H. Mabuchi. Measurement of Mesoscale Conformational Dynamics of Freely Diffusing Molecules with Tracking FCS. *Biophysical Journal*, 114(7):1539–1550, 2018.

[7] M. Piliarik and V. Sandoghdar. Direct optical sensing of single unlabelled small proteins and super-resolution imaging of their binding sites. *Nature Communications*, pages 1–8, 2014.

[8] R. W. Taylor and V. Sandoghdar. Interferometric scattering microscopy: Seeing single nanoparticles and molecules via rayleigh scattering. *Nano Letters*, 19:4827–4835, 2019.

[9] P. Kukura, H. Ewers, C. Müller, A. Renn, A. Helenius, and V. Sandoghdar. High-speed nanoscopic tracking of the position and orientation of a single virus. *Nature Methods*, 6(12):923–927, 2009.

[10] E. M. Larsson, S. Syrenova, and C. Langhammer. Nanoplasmonic sensing for nanomaterials science. *Nanophotonics*, 1:249–266, 2012.

[11] S. Unser, I. Bruzas, J. He, and L. Sagle. Localized surface plasmon resonance biosensing: Current challenges and approaches. *Sensors*, 15:15684–15716, 2015.

[12] N. P. Mauranyapin, L. S. Madsen, M. A. Taylor, M. Waleed, and W. P. Bowen. Evanescent single-molecule biosensing with quantum-limited precision. *Nature Photonics*, 11(8):477–481, 2017.

[13] F. Vollmer and L. Yang. Label-free detection with high-q microcavities: a review of biosensing mechanisms for integrated devices. *Nanophotonics*, 1:267–291, 2012.

[14] M. R. Foreman, J. D. Swaim, and F. Vollmer. Whispering gallery mode sensors. *Optics Review*, 7:168–240, 2015.

[15] F. Vollmer, S. Arnold, and D. Keng. Single virus detection from the reactive shift of a whispering-gallery mode. *Proceedings of the National Academy of Sciences of the United States of America*, 105(52):20701–20704, 2008.

[16] M. D. Baaske and F. Vollmer. Optical observation of single atomic ions interacting with plasmonic nanorods in aqueous solution. *Nature Photonics*, 10(11):733–739, 2016.

[17] J. Su, A. F. G. Goldberg, and B. M. Stoltz. Label-free detection of single nanoparticles and biological molecules using microtoroid optical resonators. *Light: Science and Applications*, 5(August 2015):2–7, 2016.

[18] T. Lu, H. Lee, T. Chen, S. Herchak, J. H. Kim, S. E. Fraser, R. C. Flagan, and K. Vahala. High sensitivity nanoparticle detection using optical microcavities. *Proceedings of the National Academy of Sciences of the United States of America*, 108(15):5976–5979, 2011.

[19] J. Zhu, S. K. Ozdemir, Y.-F. Xiao, L. Li, L. He, D.-R. Chen, and L. Yang. On-chip single nanoparticle detection and sizing by mode splitting in an ultra-high-q microresonator. *Nature Photonics*, 4:46–49, 2009.

[20] A. A. P. Trichet, J. Foster, N. E. Omori, D. James, P. R. Dolan, G. M. Hughes, C. Vallance, and J. M. Smith. Open-access optical microcavities for lab-on-a-chip refractive index sensing. *Lab on a Chip*, 14(21):4244–4249, 2014.

[21] A. A. P. Trichet, P. R. Dolan, D. James, G. M. Hughes, C. Vallance, and J. M. Smith. Nanoparticle Trapping and Characterization Using Open Microcavities. *Nano Letters*, 16(10):6172–6177, 2016.

[22] M. Mader, J. Reichel, T. W. Hänsch, and D. Hunger. A scanning cavity microscope. *Nature Communications*, 6:1–7, 2015.

[23] H. Kelkar, D. Wang, D. Martín-Cano, B. Hoffmann, S. Christiansen, S. Götzinger, and V. Sandoghdar. Sensing nanoparticles with a cantilever-based scannable optical cavity of low finesse and sub- $\lambda 3$ volume. *Physical Review Applied*, 4(5):1–11, 2015.

[24] S. Nimmrichter, C.-F. Chen, B. B. Klopfer, M. A. Kasevich, and T. Juffmann. Full-field cavity enhanced microscopy techniques. *Journal of Physics: Photonics*, 1(1):015007, 2018.

[25] P. Horak, H. Ritsch, T. Fischer, P. Maunz, T. Puppe, P. W. Pinkse, and G. Rempe. Optical kaleidoscope using a single atom. *Physical Review Letters*, 88(4):436011–436014, 2002.

[26] D. Hunger, T. Steinmetz, Y. Colombe, C. Deutsch, T. W. Hänsch, and J. Reichel. Fiber fabry-perot cavity with high finesse. *New Journal of Physics*.

[27] D. Hunger, C. Deutsch, R. J. Barbour, R. J. Warburton, and J. Reichel. Laser micro-fabrication of concave, low-roughness features in silica. *AIP Advances*, 2:012119, 2012.

Figures

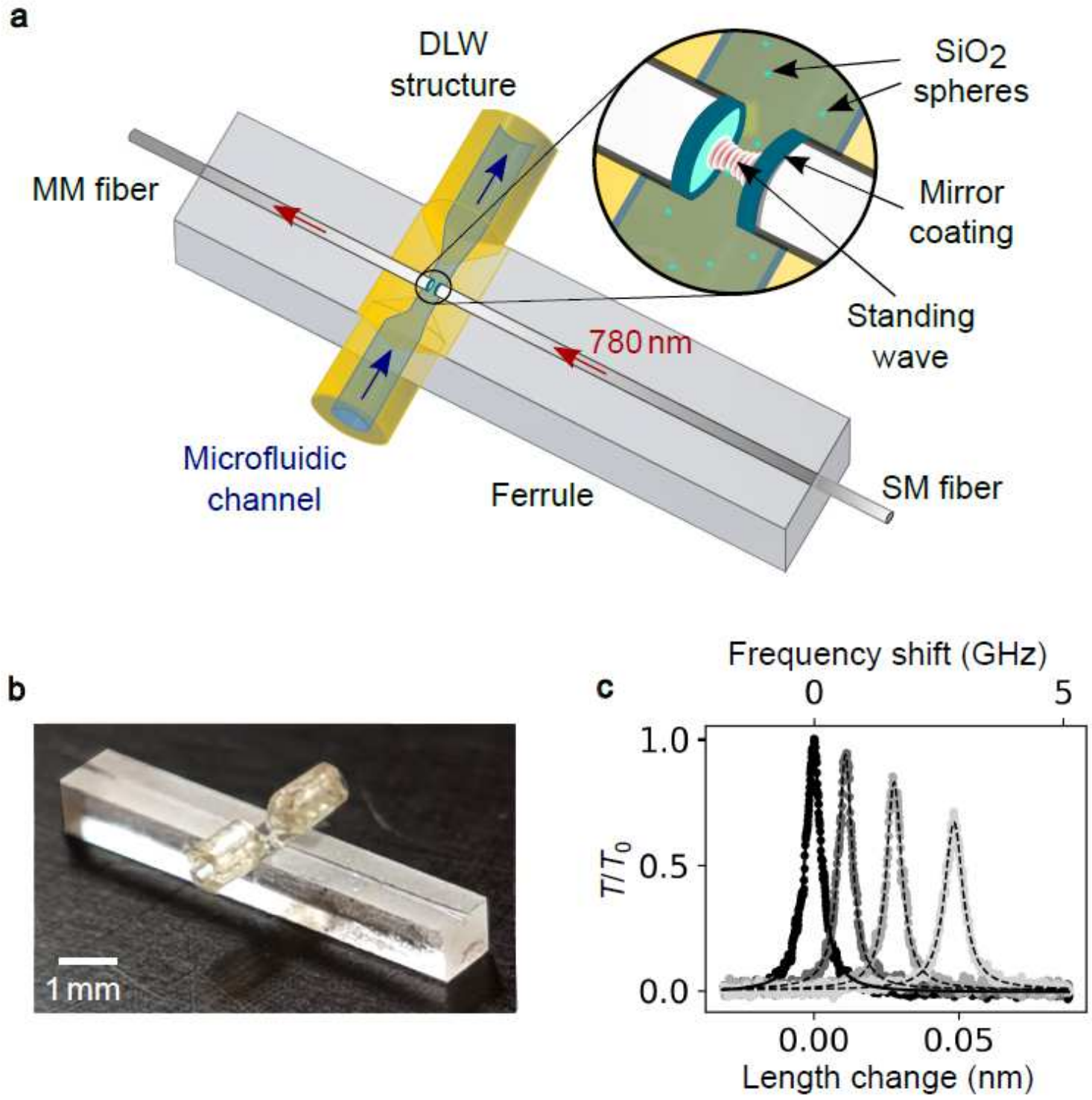

Figure 1

Fabry-Perot microcavity device and measurement signal. (a) Schematic setup showing the cavity and its integration into a glass ferrule with a direct-laser-written (DLW) structure (yellow) forming the microfluidic channel. b) Picture of the microfluidic device. c) Examples of the cavity transmission signal for an empty cavity (black) and with nanoparticles present at increasing spatial overlap with the cavity mode

(decreasing gray value). The increasing frequency shift, decreasing peak transmission, and increasing linewidth are visible.

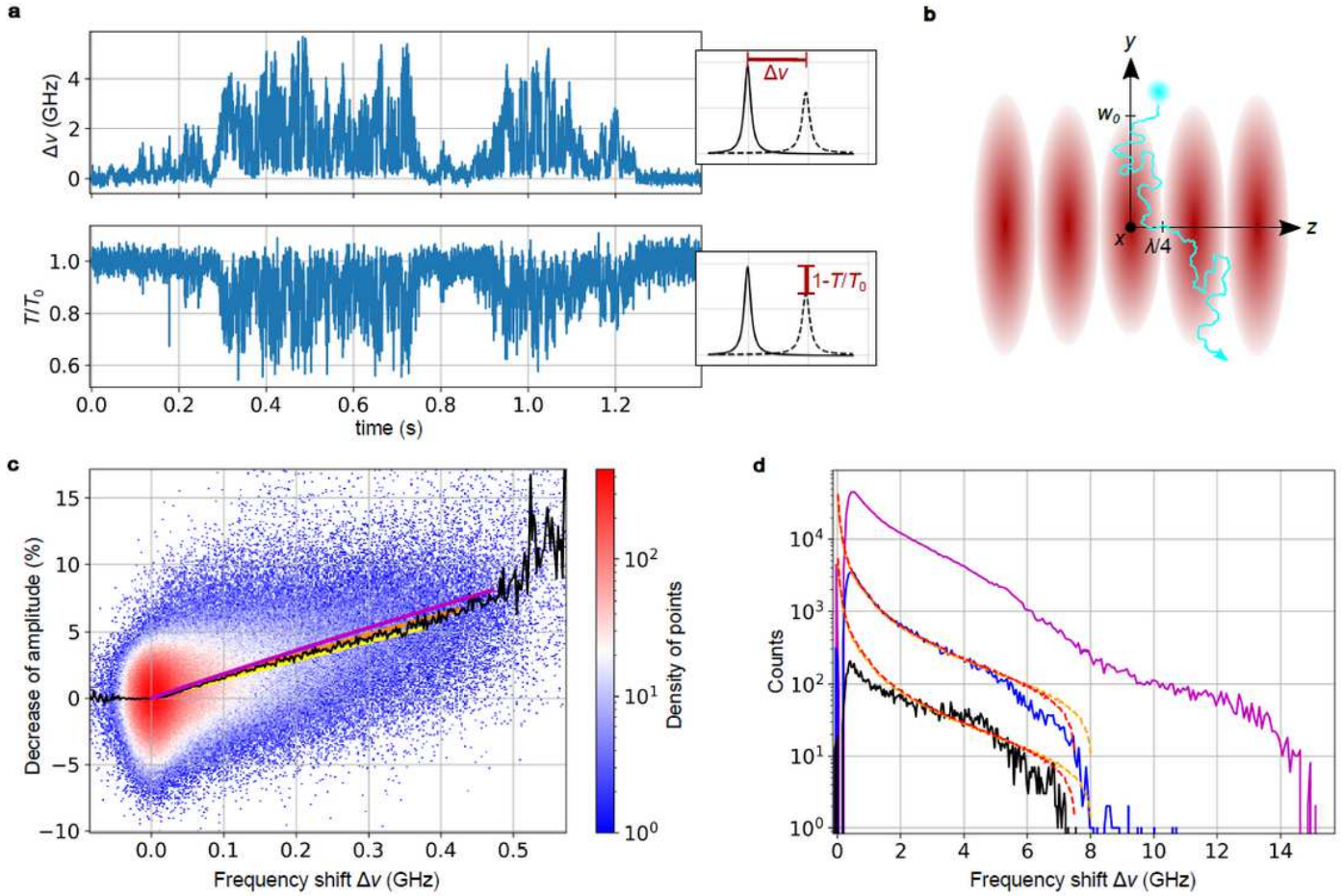

Figure 2

Quantitative nanoparticle characterization. a) Cavity frequency shift and peak transmission amplitude as a function of time produced by a single SiO2 nanoparticle. b) Schematic sketch of a nanoparticle diffusing through the standing wave cavity field. c) Statistical correlation of cavity frequency shifts and transmission reductions. Solid black line: Mean transmission reduction for a given frequency shift. Solid yellow line: simulation for np = 1.41, orange: np = 1.42; purple: np = 1.43. d) Histograms for the measured frequency shifts of a single transit event (black data) shown in Fig. 3b, 59 transits (blue data, measurement duration: 2 hours) and 210 additional transits (magenta data, 8 hours). The observed increased shifts reveal agglomeration. Dashed lines: simulation for np = 1.46 and the mean radius of rhydr = 75.3 nm (red) and the maximal radius of rhydr = 77.2 nm (orange).

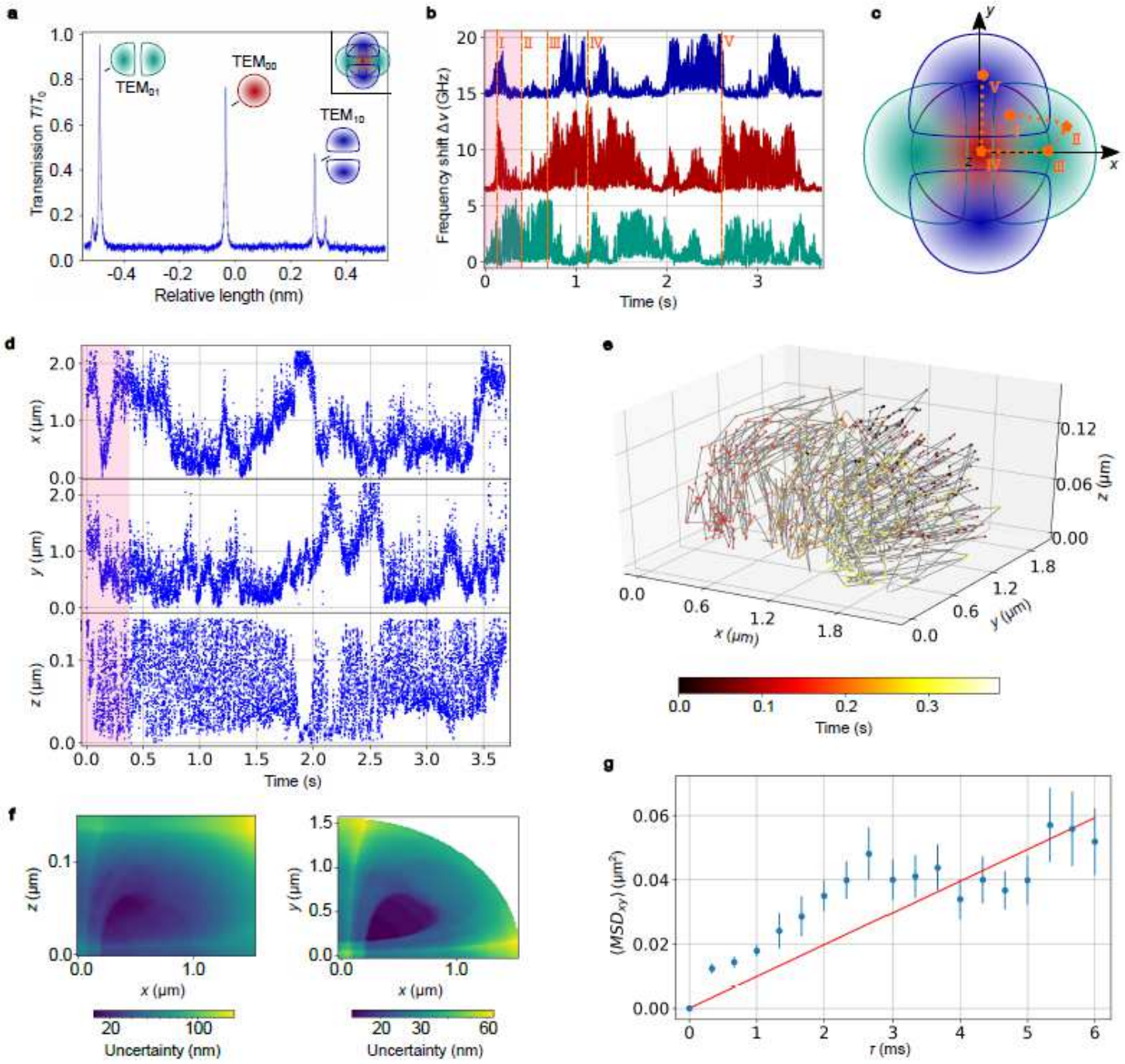

Figure 3

Three-dimensional tracking of a single SiO2 nanosphere and determination of its diffusivity. a) Cavity transmission signal with the three evaluated modes indicated. Inset: Schematic illustration of the complementary spatial regions covered by the modes. b) Time trace of frequency shifts of the three modes. c) Sketch for different particle positions at different times depicted in 3b) d) Evaluated positions for shortest distance algorithm. e) Two-dimensional representation of the position tracking. f) Lateral resolution for different positions. g) Mean squared displacement for the lateral diffusion and weighted linear fit. The error bars represent the standard deviation.

Supplementary Files

This is a list of supplementary files associated with this preprint. Click to download.

- SupplementaryInformationLKMMCKMWDHLineNumbers.pdf